Journal of The Electrochemical Society, **155** (7) A542-A552 (2008)
0013-4651/2008/155(7)/A542/11/$23.00 © The Electrochemical Society

Intercalation-Induced Stress and Heat Generation within Single Lithium-Ion Battery Cathode Particles

Xiangchun Zhang,[a,*] Ann Marie Sastry,[a,b,c,,z] and Wei Shyy[d]**

[a]*Department of Mechanical Engineering,* [b]*Department of Materials Science and Engineering,* [c]*Department of Biomedical Engineering, and* [d]*Department of Aerospace Engineering, University of Michigan, Ann Arbor, Michigan 48109, USA*

Intercalation-induced stress and heat generation inside Li-ion battery cathode ($LiMn_2O_4$) particles under potentiodynamic control are simulated in this paper. We combined analyses of transport and kinetics in determining resulting stresses, which arise from concentration gradients in cathode particles, and heat generation. Two peaks in boundary reaction flux, and resulting stresses, were determined from the modeling of electrochemical kinetics and diffusion, using intrinsic material properties (resulting in two plateaus in the open-circuit potential) and the applied potential. Resistive heating was identified as the most important heat generation source. To probe the impact of the particle shape (equivalent radius and aspect ratio of an ellipsoidal particle) and the potential sweep rate on stress and heat generation, a surrogate-based analysis was also conducted. The systematic study showed that both intercalation-induced stress and time-averaged resistive heat generation rate increase with particle radius and potential sweep rate. Intercalation-induced stress increases first, then decreases as the aspect ratio of an ellipsoidal particle increases, whereas time-averaged resistive heat generation rate decreases as aspect ratio increases. This surrogate-based analysis suggests that ellipsoidal particles with larger aspect ratios are preferred over spherical particles, in improving battery performance when stress and heat generation are the only factors considered.
 [DOI: 10.1149/1.2926617]

Manuscript submitted January 30, 2008; revised manuscript received April 21, 2008. Available electronically May 23, 2008.

Excessive heat generation in Li batteries, resulting in thermal runaway, results in complete cell failure accompanied by violent venting and rupture, along with ignition of battery active materials.[1-4] Stress-induced fracture also putatively degrades performance in these cells, as evidenced by observation of fractured surfaces in postmortem analysis of batteries.[5-7] Stress generation results from lithium-ion extraction from the cathode (deintercalation), transport across the electrolyte, and insertion into the anode (intercalation), and the reverse reaction.[8] Intercalation-induced stress varies cyclically, and thus, damage aggregates with usage.[5] Particle-scale fracture of active materials results in performance degradation of batteries, due to the loss of electrical contact, and subsequent increase in the surface area subjected to side reactions.[9] These phenomena, heat and stress generation, undoubtedly amplify one another, and both phenomena are governed by cell kinetics. Inclusion of heat generation, mechanical stresses, and chemical kinetics in models at critical scales (i.e., particle scales), appears necessary, and progress in each is discussed in order.

It is important to distinguish between heat transfer and heat generation analyses in battery materials. We use "heat generation" to refer to the sources of heat in the cell; "heat transfer" by contrast, refers to the resulting distribution of temperature. Though the sources of heat generation may be readily determined, solution for the distribution of temperature requires an even more detailed understanding of both geometry and material properties, as will be discussed later. Heat transfer analyses of lithium-ion batteries have stemmed from work on full cells.[10] This classic work[10] was later extended to consider the effect of lithium concentration in intercalation compounds.[1] Foci of subsequent studies have mainly been on improved modeling of heat transfer rather than refinement of geometric models to the particle scale. A three-dimensional (3D) model was developed, considering anisotropic conductivity, to simulate the temperature distribution inside lithium polymer batteries under galvanostatic discharge, for a dynamic power profile.[11] Later, a layer-wise 3D model (assuming different conductivities for each homogeneous layer), was derived,[12] in which radiation and convection were considered.

Thus, progress to date in heat transfer modeling has been restricted to consideration of continuum layers, though modeling at the particle scale appears necessary at this time, given our ability to select particle geometry within electrodes. Meanwhile, models have appeared in intercalation-induced stress, which do address the particle scale, e.g., a one-dimensional model to estimate stress generation within spherical electrode particles[13] and a two-dimensional model to predict electrochemically induced stresses.[14] Neither, however, has considered complex particle shapes or the effect of layer-wise thickness on critical percolation limits.[15] In more recent work,[16] a 3D model based on a thermal stress analogy has been used to simulate the intercalation-induced stress inside cathode particles, but without consideration of electrochemical kinetics.

In order to fully and predictively link thermal and stress-induced failures, kinetic effects must also be understood, in tandem with detailed models of electrode architecture, in three dimensions, and for complex particle shape. Though it has been established that microscopic features of structures in batteries, including particle shape and size distributions, are important factors in battery performance,[17] models have not been reported that incorporate electrochemical kinetics. Thus, in the present work, we model a $LiMn_2O_4$ cathode particle under potentiodynamic control, with linearly variable applied potential to the particle.[18,19] The cathode particle was assumed to be homogeneous. We had the following specific objectives:

1. To develop and numerically implement particle scale models to simulate intercalation-induced stress and heat generation, and to interrogate the interactions among intercalation, stress, and heat generation, for spherical particles.
2. To understand how stress and heat generation depend on the ratio of axial lengths for ellipsoidal cathode particles, operating conditions, and with discharge time, using surrogate-based analysis.

Our general methodology comprised two sequential efforts. First, we developed a model that physically links intercalation-induced stress and thermal stress, following prior work.[16] Three distinct sources of heat generation were considered, namely, heat of mixing, entropic heat, and resistive heating.[1] Though heat generation at this scale is different, we do not at present have sufficient information on local heat transfer coefficients within anisotropic particles to properly model heat transfer, and thus, determination of localized temperature distribution via heat transfer analysis is not attempted here. Implementation of the model requires physical parameters, including partial molar volume,[16] Young's modulus,[16] and the derivative of open-circuit potential (OCP) over temperature.[20]

* Electrochemical Society Student Member.
** Electrochemical Society Active Member.
z E-mail: amsastry@umich.edu

Table I. Representative cathode compositions and particle sizes.

Active material	Binder	Additives	Ref.
$LiFePO_4$ 76–88 wt %	PVdF 12 wt %	Carbon black 0–10 wt % graphite 0–6 wt %	28
$LiMn_2O_4$ 81.5 wt %	PVdF 10 wt %	Carbon black 8.5 wt %	25
$LiMn_2O_4$ 80 wt %	Ethylene propylene diene terpolymer 5 wt %	Carbon black 15 wt %	26
Active material	**Synthesis method**	**Sizes**	**Ref.**
$LiMn_2O_4$	Calcination from Mn_3O_4 and Li_2CO_3	Crystalline grain: ca. nanometers Primary particle: ca. 3–4 μm	22
$Li[Mn_{1/3}Ni_{1/3}Co_{1/3}]O_2$	Carbonate Coprecipitation method at 950°C	Primary particle: ca. 1 μm Secondary particle: ca. 11 μm	30
$LiFePO_4$	Microwave processing	Primary particle: ca. 0.3 μm Secondary particle: ca. 20–60 μm	31

The second effort, in surrogate modeling, comprised the use of surrogate models to analyze relationships among stress and heat generation, and ellipsoidal particle morphology and operating conditions. We first conducted simulations on selected training points in critical regions using the models developed to obtain the stress and heat generation. The simulation results were then approximated by surrogate models, which were used after validation, for further analysis of stress and heat generation for different particle geometries and cycling rates.

Electrochemical, Mechanics, and Thermal Modeling

In lithium-ion batteries, actual cathode particle morphology varies with synthesis methods.[21-24] Primary particles, made of crystalline grains, are agglomerated using polymeric binders [e.g., poly (vinylidene fluoride) (PVdF)][2,25] and incorporating conductive additives, such as carbon black,[25,26] nonaqueous ultrafine carbon suspensions,[27] and graphite,[28,29] to form secondary particles. Typical cathode compositions and particle sizes are shown in Table I.[22,25,26,28,30,31] Sizes range from 0.3 to 4 μm for primary particles and 11–60 μm for secondary particles.

Modeling of these aggregates at the scale of single crystals requires molecular or atomistic simulations. Thus, we restrict our considerations in the present paper to a pure active material ($LiMn_2O_4$) without inclusions. Our model cathode particles are homogeneous, isotropic single-phase ellipsoidal particles (prolate spheroids) or spherical particles. The stress localization due to interaction between the crystalline grains is not considered in stress generation simulations, and the temperature inside a particle is assumed to be uniform in heat generation simulations.

Determination of intercalation-induced stress and heat generation first requires mapping of concentration distribution and current density. Concentrations are obtained by solving the diffusion equation with appropriate boundary conditions for each case (see next section). To model the intercalation-induced stress, a constitutive equation is used to relate intercalation-induced strain. A heat generation model developed for a whole cell[1] is used here because our simulations rely on the assumption that the cathode particle behaves as one electrode of a whole cell, incorporating experimental parameters from microelectrode studies,[18] wherein a single cathode electrode and the counter electrode (lithium foil) comprise the electrochemical cell.

Model of intercalation.— An intercalation process can ideally be modeled as a diffusion process with boundary flux determined by electrochemical reaction rate. The model of the intercalation process presented in this section includes a Li-ion transport equation and a boundary condition determined by the electrochemical kinetics on the particle surface under potentiodynamic control.

Li-ion transport equation.— Li-ion diffusion is driven by chemical potential gradient. For a given concentration and stress gradients, the diffusion flux is given by[16]

$$\mathbf{J} = -D\left(\nabla c - \frac{\Omega c}{RT}\nabla \sigma_h\right) \quad [1]$$

where c is the concentration of Li-ion, σ_h is the hydrostatic stress, defined as $\sigma_h = (\sigma_{11} + \sigma_{22} + \sigma_{33})/3$ (where σ_{ij} is the element in stress tensor), D is diffusion coefficient, R is general gas constant, and T is temperature. With substitution of Eq. 1 into the mass conservation equation, we obtain the species transport equation as follows[16]

$$\frac{\partial c}{\partial t} + \nabla \cdot \left[-D\left(\nabla c - \frac{\Omega c}{RT}\nabla \sigma_h\right)\right] = 0 \quad [2]$$

The boundary condition for this equation is that the flux on the particle surface is related to the discharge/charge current density $\mathbf{i}_n$ as

$$\mathbf{J} = -D\left(\nabla c - \frac{\Omega c}{RT}\nabla \sigma_h\right) = \frac{\mathbf{i}_n}{F} \quad [3]$$

where F is Faraday's constant.

Electrochemical kinetics under potentiodynamic control.— The current density on the particle surface depends on the electrochemical reaction rate. The reactions at the positive electrode are

$$LiMn_2O_4 \Leftrightarrow Li_{1-x}Mn_2O_4 + xLi^+ + xe^-$$

During charge, the positive electrode is oxidized and lithium ions are extracted from the positive electrode particle. During discharge, the positive electrode is reduced and lithium ions are inserted into the positive electrode particle. Chemical kinetics (reaction rate) are described by the Butler–Volmer equation,[32,33] as

$$J = \frac{i_n}{F} = \frac{i_0}{F}\left\{\exp\left[\frac{(1-\beta)F}{RT}\eta\right] - \exp\left[-\frac{\beta F}{RT}\eta\right]\right\} \quad [4]$$

where i_0 is exchange current density, η is surface overpotential, and β is symmetry factor, which represents the fraction of the applied potential that promotes the cathodic reaction.[33]

The exchange current density i_0 is given by

$$i_0 = Fk(c_l)^{1-\beta}(c_\theta)^{1-\beta}(c_s)^{\beta} \quad [5]$$

where c_l is the concentration of lithium ion in the electrolyte, c_s is the concentration of lithium ion on the surface of the solid electrode, c_θ is the concentration of available vacant sites on the surface ready for lithium intercalation (which is the difference between stoichiometric maximum concentration and current concentration on the sur-

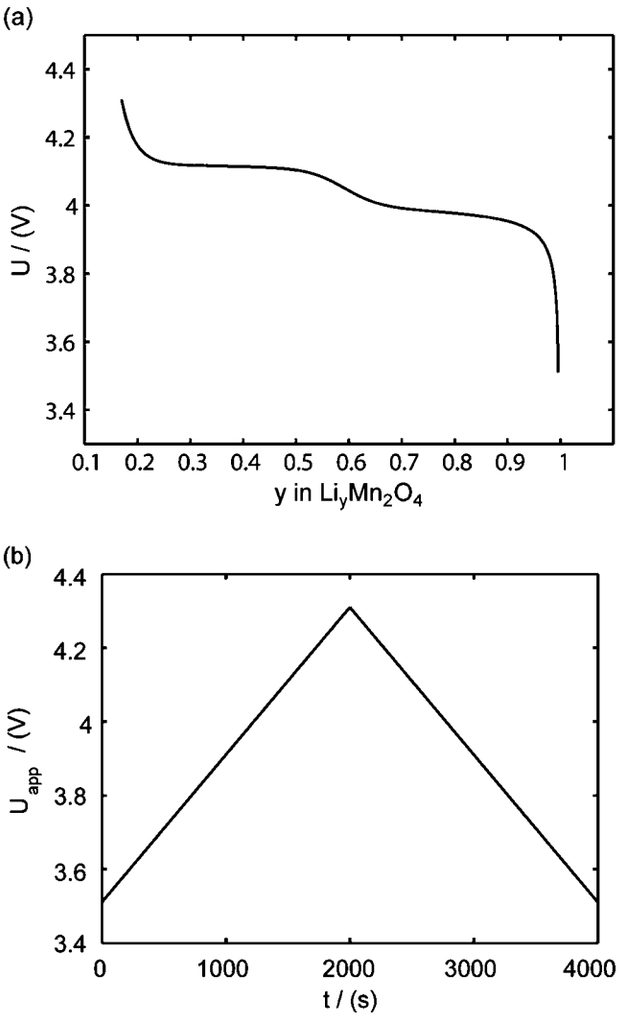

Figure 1. Potentials: (a) OCP of $LiMn_2O_4$ and (b) applied potential sweeping profile during one cycle.

face of the electrode $c_{max} - c_s$), and k is a reaction rate constant.[32]

In Eq. 4, the surface overpotential is the difference between the potential of the solid phase (compared to the electrolyte phase) V and OCP U[32]

$$\eta = V - U \quad [6]$$

A fit of the experimental results[34] of OCP for $LiMn_2O_4$ is illustrated in Fig. 1a. OCP depends on the state of charge y (i.e., the atomic ratio of lithium in the electrode $Li_yMn_2O_4$); this is a measure of the lithium concentration in the electrode. As shown in Fig. 1a, there are two plateaus in the potential distribution, resulting from the ordering of the lithium ions on one-half of the tetrahedral 8a sites of $LiMn_2O_4$.[35] Following the numerical study,[19] the potential of the solid phase is assumed, because of the small size of particles, to be uniform within each particle, having the value of the applied potential

$$V = U_{app} \quad [7]$$

when under microvoltammetric study (for example, Ref. 18). This assumption of a uniform potential distribution will be evaluated in a later section. Under potentiodynamic control, the applied potential changes linearly with time,[18,19] for the fixed potential sweep rate v. Once the applied potential reaches the upper bound, the potential sweep rate changes sign to sweep backward. Figure 1b shows an example of the potential sweep, with $v = 0.4$ mV/s. Increasing applied potential, in the first half cycle, drives the charging process, while the decreasing applied potential, in the second half cycle, drives the discharging process. As the potential cycles between 3.5102 and 4.3102 V,[19] the electrode particle is thus charged and discharged.

Table II. Parameters and material properties for the intercalation model (where r_0 is the radius of a spherical particle).

Symbol	Value
β	0.5
c_l	1000 mol/m^{3a}
c_{max}	2.37×10^4 mol/m^{3a}
k	1.9×10^{-9} m$^{5/2}$ s^{-1} mol$^{-1/2a}$
D	2.2×10^{-9} cm^2/s^a
v	0.4 mV/s
r_0	5 μm

[a] Ref. 19

For this applied potential stimulus, the initial condition for the species transport equation (Eq. 2) is $c|_{t=0} = c_0 = 0.996c_{max}$.

Parameters and material properties.— A reasonable way to obtain the lithium-ion concentration in the electrolyte c_l would be to solve the species transport equation in the electrolyte. However, it is assumed to be a constant value in this study following Ref. 19. The values of parameters and material properties used in this study (unless otherwise stated) are listed in Table II.

Intercalation-induced stress model.— The constitutive equation between stress and strain, including the effect of intercalation-induced stress by the analogy to thermal stress, is

$$\varepsilon_{ij} = \frac{1}{E}[(1+\nu)\sigma_{ij} - \nu\sigma_{kk}\delta_{ij}] + \frac{\tilde{c}\Omega}{3}\delta_{ij} \quad [8]$$

where ε_{ij} are strain components, σ_{ij} are stress components, E is Young's modulus, ν is Poisson's ratio, $\tilde{c} = c - c_0$ is the concentration change of the diffusion species (lithium ion) from the original (stress-free) value, and Ω is the partial molar volume of lithium.[16] Stress components are subjected to the force equilibrium equation

$$\sigma_{ij,i} = 0 \quad (j = 1,2,3) \quad [9]$$

A Young's modulus $E = 10$ GPa and a partial molar volume $\Omega = 3.497 \times 10^{-6}$ m^3/mol[16] are assumed here. Equations 2 and 8 are coupled through concentration c and stress σ_h.

Heat generation model.— There are four sources of heat generation inside lithium-ion batteries during operation[1]

$$\dot{Q}_g = I(V - U^{avg}) + IT\frac{\partial U^{avg}}{\partial T} + \sum_k \Delta H_k^{avg} r_k + \int \sum_j \sum_i (\bar{H}_{ij} - \bar{H}_{ij}^{avg})\frac{\partial c_{ij}}{\partial t} dv \quad [10]$$

The first term, $I(V - U^{avg})$, is the irreversible resistive heating, where I is the current of the cell, V is the cell potential, and U^{avg} is the volume averaged OCP. Resistive heating is caused by the deviation of the cell potential from its equilibrium potential by resistance to the passage of current. The second term, $IT\,\partial U^{avg}/\partial T$, is the reversible entropic heat, where T is temperature. The third term, $\Sigma_k \Delta H_k^{avg} r_k$, is the heat change of chemical side reactions, where ΔH_k^{avg} is the enthalpy of reaction for chemical reaction k, and r_k is the rate of reaction k. The fourth term, $\int \Sigma_j \Sigma_i (\bar{H}_{ij} - \bar{H}_{ij}^{avg})\,\partial c_{ij}/\partial t dv$, is the heat of mixing due to the generation and relaxation of concentration gradients, where c_{ij} is the concentration of species i in phase j, dv is the differential volume element, and $\bar{H}_{ij}$

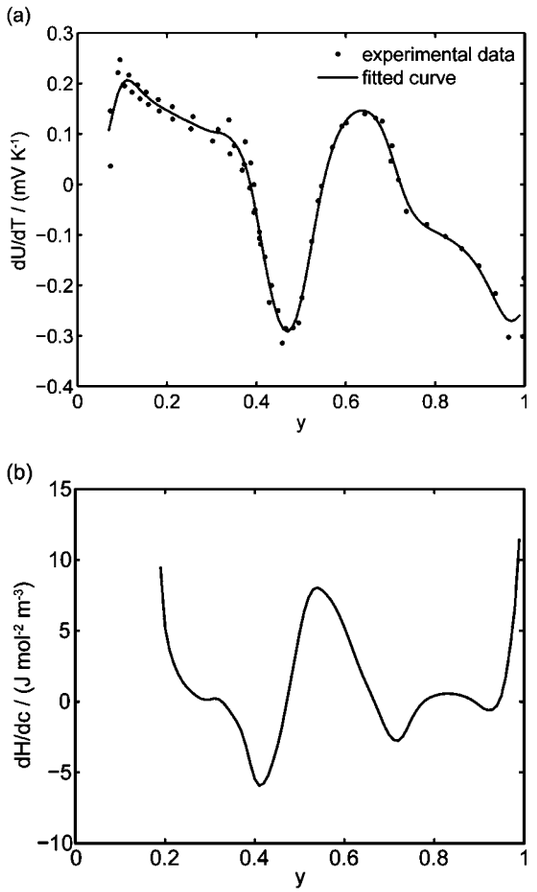

Figure 2. Material properties: (a) The derivative of OCP over temperature dU/dT: curve fitting of the measured data from Ref. 20 and (b) the derivative of partial molar enthalpy over concentration obtained by $\partial\bar{H}/\partial c = -F\,\partial\,(U - T du/dT)/\partial c$ based on the curve fit in (a).

and $\bar{H}_{ij}^{\text{avg}}$ are partial molar enthalpy of species i in phase j and the averaged partial molar enthalpy, respectively.

The charge/discharge current I is obtained by the integration of current density i_n (determined by electrochemical kinetics as shown in Eq. 4) over the particle surface. The potential of solid electrode V equals the applied potential, as in Eq. 7. The volume averaged OCP U^{avg} is determined by using the volume-averaged state of charge and the experimental results of OCP, as shown in Fig. 1a. $\partial U^{\text{avg}}/\partial T$ is measured concentration and is thus dependent on the state of charge. Experimental results of dU/dT for $LiMn_2O_4$ in Ref. 20 are used here. The experimental results of dU/dT from Ref. 20 are fitted by a smoothing spline method (Matlab), used commonly to characterize data with a high degree of noise.[36] Fit statistics for these data are $R^2 = 0.977$ and $R^2_{\text{adj}} = 0.967$, and with the fitted curve shown in Fig. 2a.

The term $\Sigma_k \Delta H_k^{\text{avg}} r_k$ in Eq. 10 is neglected because of the assumption of no side reactions. The heat of mixing term is simplified as[1]

$$\dot{Q}_{\text{mixing}} = \int \sum_j \sum_i (\bar{H}_{ij} - \bar{H}_{ij}^{\text{avg}}) \frac{\partial c_{ij}}{\partial t} dv = \frac{\partial}{\partial t}\left[\frac{1}{2}\frac{\partial \bar{H}_s}{\partial c_s}\int (c_s - c_{s,\infty})^2 dv\right] \quad [11]$$

by assuming that (*i*) the volume change effect can be neglected such that the temporal derivative can be taken outside the integral and (*ii*) the particle is in contact with a thermal reservoir such that temperature is constant.[1] Equation 11 suggests that heat of mixing vanishes when the concentration gradient relaxes. In Eq. 11, $\partial\bar{H}_s/\partial c_s = -F\,\partial\,U_H/\partial c_s$ where $U_H = U - T dU/dT$ is enthalpy potential. The term $\partial\bar{H}_s/\partial c_s$ is obtained by numerical differentiation of enthalpy potential U_H over concentration. First, U_H is calculated according to $U_H = U - T dU/dT$ by taking $T = 300$ K and the curve fitting results in Fig. 2a. Then, U_H is numerically differentiated over concentration and multiplied by $-F$ to obtain $d\bar{H}/dc$, plotted in Fig. 2b.

Spherical particle simulation results.— The intercalation, stress, and heat generation models described above were implemented on spherical particles with radius $r_0 = 5$ μm using the simulation tool COMSOL Multiphysics. A potential sweep rate of $v = 0.4$ mV/s was selected, giving a discharge/charge rate of 1.8 C, falling in the range of typical rates for high-power applications of lithium-ion batteries.

Intercalation-induced stress inside spherical particles.— The simulation results of reaction flux and stresses are shown in Fig. 3. Figure 3a shows the diffusion flux, determined by electrochemical kinetics, on the particle surface during one cycle of voltammetry. It is positive in the first half cycle (as lithium ions are extracted from the cathode during charge) and negative in the second half cycle (as lithium ions are inserted into the cathode during discharge). This is a similar trend to those from simulations[19] and experiments.[18] The first principal stress (radial stress) is largest at the center of the particle, and the von Mises stress is largest on the particle surface. Figure 3b shows that radial stress at the center of the particle is negative (compressive) in the first half cycle and positive (tensile) in the second half cycle. In the first half cycle, lithium ions are extracted so that the lattice contracts in the outer region of the particle. Therefore, the radial stress is compressive at the center of the particle. In the second half, lithium ions are inserted so that the lattice expands in the outer region of the particle. Therefore, the radial stress is tensile at the center of the particle in this half cycle. Figure 3c shows the time history of von Mises stress on the particle surface. The flux and stress of charge and discharge half cycles are symmetric. This is because the symmetric applied potential dominates over simulation parameters for these conditions. The distribution of flux and stress may be asymmetric when other parameters, such as potential sweep rate and symmetry factor, are dominant.

Figures 3a-c show that two peaks in species flux and stress time history arise in each half cycle. To determine the origin of these peaks, a detailed study of the first half cycle was conducted. The time history of diffusion flux and von Mises stress on the surface in the charge half cycle are replotted in Fig. 4a and b. As shown in Fig. 4a, two peaks of surface flux occur at $t = 1202$ and 1541 s, respectively. By the Butler–Volmer equation for electrochemical kinetics on particle surface (Eq. 4), surface flux depends on surface overpotential η and exchange current density i_0. Surface overpotential η is the difference between the applied potential and the OCP as shown in Eq. 6 and 7. The applied potential increases linearly with time in the charge half cycle of the potentiodynamic process, as illustrated in Fig. 1b. The OCP changes with the lithium content in the electrode, as shown in Fig. 1a. During the charging process, OCP increases as lithium concentration decreases. The difference between the two increasing potentials surface overpotential is shown in Fig. 4c. It is shown in Fig. 4c that there are two peaks in the surface overpotential plot mainly due to the two plateaus in the OCP in Fig. 1a. Because surface overpotential appears in the exponential terms in Eq. 4, it is the dominant factor for the resulting flux. Therefore, there are two peaks in the flux plot as shown in Fig. 4a. However, a closer look at the time instants for the peaks in Fig. 4a and c shows that the corresponding peaks appear at different times. This is attributable to the temporal distribution of exchange current density (as plotted in Fig. 4d) because the flux is actually the product of exchange current density and the exponential terms, including surface overpotential, as shown in Eq. 4. To summarize, the peaks in the

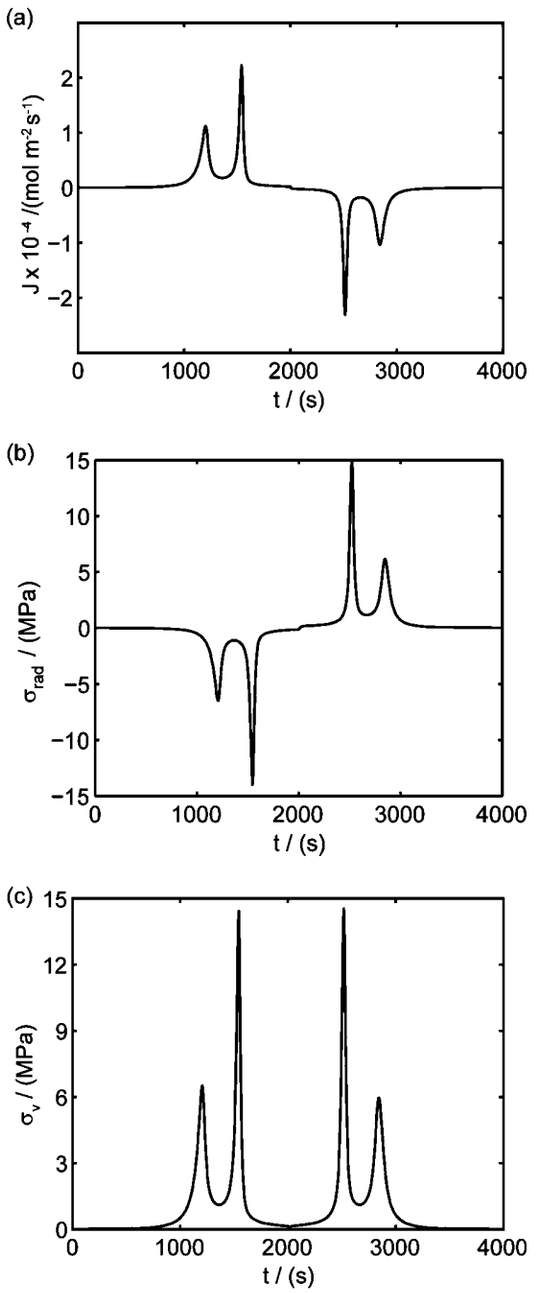

Figure 3. Simulation results of a spherical particle with $v = 0.4$ mV/s, $r_0 = 5$ μm: (a) Diffusion flux on the particle surface, (b) radial stress at the center of the particle, and (c) von Mises stress on the particle surface.

flux distribution originate essentially from the two plateaus in the OCP distribution, which is an intrinsic property of the cathode material $LiMn_2O_4$, and the temporal variation of the applied potential.

To explain the peaks in the stress plot in Fig. 4b, we recall the expression of the von Mises stress on a spherical particle surface (von Mises stress has its maximum value on the particle surface $r = r_0$)[16]

$$\sigma_v(r = r_0) = |\sigma_{rad} - \sigma_{tang}|_{r=r_0} = \frac{\Omega E}{3(1-\nu)}\left[\frac{3}{r_0^3}\int_0^{r_0} \tilde{c} r^2 dr - \tilde{c}(r = r_0)\right] \quad [12]$$

As shown in Eq. 12, the von Mises stress on the particle surface depends on the difference between the global average concentration $3(\int_0^{r_0} \tilde{c} r^2 dr)/r_0^3$ and the local concentration of lithium ions. Figure 5 shows the distribution of concentrations at different times during charge. It may be seen that the concentration is quite uniformly distributed, most of the time. At $t = 1205$ and 1544 s, significant gradients are present in the concentration distribution (due to the two peak fluxes shown in Fig. 4a); therefore, we expect a predominantly large stress at these times by Eq. 12, explaining the two peaks shown in Fig. 4b. By comparing Fig. 4a and b, we also see that the peaks in the stress plot are a few seconds later than the corresponding peaks in the flux plot. This is because it takes time for the concentration distribution to respond to the change of the boundary flux in the diffusion process. The peaks in the radial stress plot in Fig. 3b can be explained similarly, by considering the fact that radial stress depends on the difference between the global and local average of concentrations,[16] the nonuniformity of the concentration distribution.

The above analysis shows that surface flux, concentration, and stress are highly interrelated. Surface flux by electrochemical reaction and diffusion determine the concentration distribution, which, in turn, affects the OCP, the chemical kinetics, and thus, surface flux. Concentration distribution determines stress, the gradient of which in turn enhances the diffusion[16] because of the effect of stress gradient on diffusion as shown in Eq. 1. The two peaks observed in the resulting flux and stress generation is attributable to the material property of $LiMn_2O_4$ (two plateaus in the OCP) and the applied potential.

Intercalation-induced stress inside spherical particles under a higher rate of charge (20 C).— A single simulation was also conducted for a spherical particle under a very high charge rate, 20 C. The spherical particle radius was 5 μm, and the potential sweep rate was increased to 4.4444 mV/s. The time history of simulated surface reaction flux and von Mises stress on the particle surface is shown in Fig. 6.

For this faster charge rate, the patterns of flux and stress time history in Fig. 6 are different from those for 1.8 C, as shown in Fig. 4, because the kinetics differ at the higher rate. Also, the peak value of surface reaction flux is 9.48×10^{-4} mol/m^2 s, which is about five times larger than the peak flux of 2.22×10^{-4} mol/m^2 s for 1.8 C charge. Figure 6 also shows that the resulting stress (peak value) increases from 14.5 to 54.4 MPa when the charge rate increases from 1.8 to 20 C.

Heat generation inside spherical particles.— The time history of each heat generation term in charge half cycle is shown in Fig. 7. The entropic heat and heat of mixing change signs during the charge half cycle, which is mainly attributable to the variation of material properties dU/dT and $d\bar{H}/dc$ from experiment measurements.

Table III gives the time-averaged rate of each heat generation term during the charging process for two different potential sweep rates. The heat of mixing is negligible compared to resistive heat and entropic heat. Entropic heat is reversible; thus, the heat generation due to this term is expected to cancel out during the charge and discharge half cycles. Therefore, the only term of interest is the resistive heat. Furthermore, resistive heat increases when the charge half cycle gets faster, which is expected because the polarization is larger for higher charge rates.

Surrogate-Based Analysis of Ellipsoidal Particles under Different Cycling Rates

To understand how stress and heat generation behave with the particle geometric configuration and the operating condition, a surrogate-based analysis approach is used. Surrogate models, which are constructed using the available data generated from preselected designs, offer an effective way of evaluating geometrical and physical variables. The key steps of surrogate modeling include design of experiments, running numerical simulations (computer experiments), construction of surrogate models, validation, and further refinement, if necessary, of the models.[37-39]

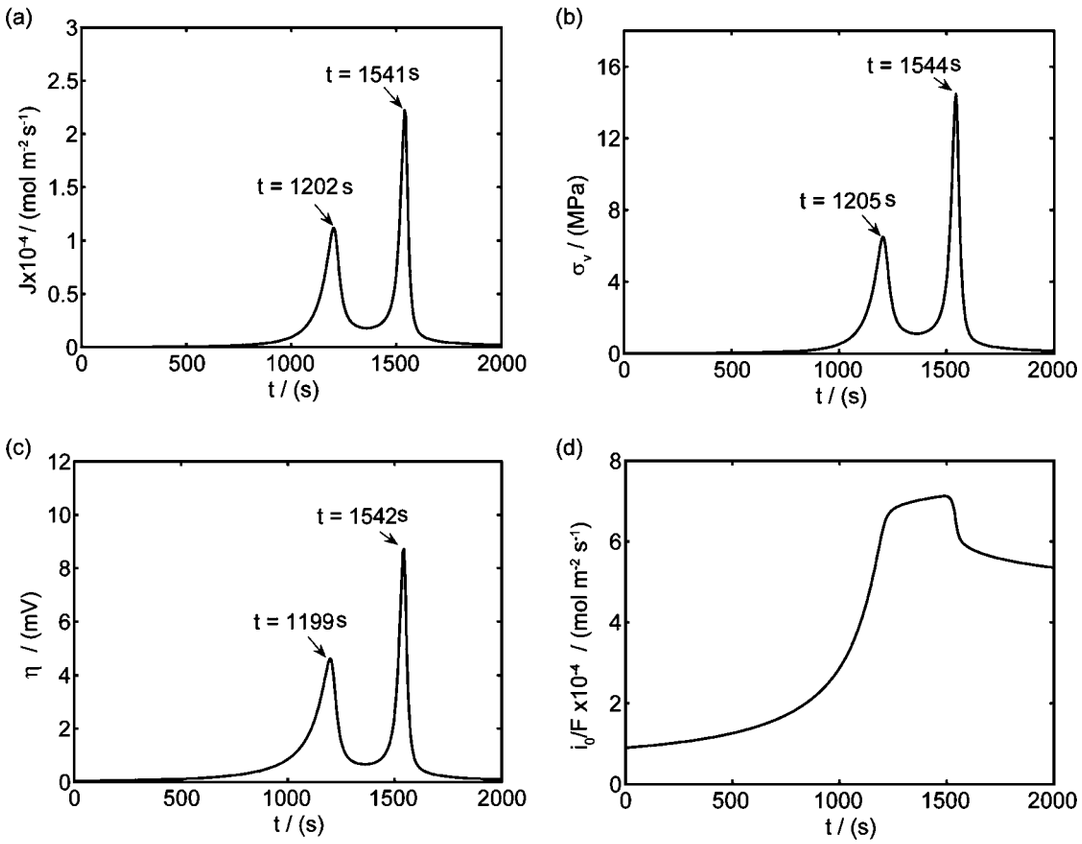

Figure 4. Simulation results of a spherical particle in the charge half cycle (v = 0.4 mV/s, r_0 = 5 μm): (a) Reaction flux on the particle surface, (b) von Mises stress on the particle surface, (c) surface overpotential, and (d) exchange current density (divided by Faraday's constant).

The design of experiments is the sampling plan in the design variable space. There are several approaches available in the literature. The combination of face-centered composite design (FCCD)[40] and Latin hypercube sampling (LHS)[41] was used here. After obtaining the sampling points in the design variable space, numerical simulations (computer experiments) were run at selected training points to obtain the value of objective variables. With simulation results for the training points, surrogate models were constructed to approximate the objective functions. Surrogate models available include polynomial regression model, krigging modeling, and radial basis functions, among others.[37] A second-order polynomial regression model was used in this study; the least-squares method was used to find the coefficients of the approximation. After constructing the response surface approximation, error estimations were necessary to validate the performance of the approximation. Common error measures used are root-mean-square (rms) error, prediction error sum of squares (PRESS), and (adjusted) coefficients of multiple determination R^2_{adj}.[42] The validated surrogate models were used for further analysis of the dependency between the objective functions and design variables to understand the underlying physics mechanisms.

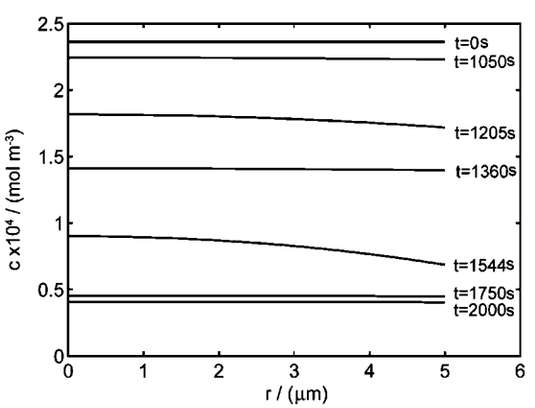

Figure 5. Distribution of lithium-ion concentration inside a spherical particle at different time instants during the charge half cycle.

Selection of variables and design of experiments.— Three design variables were selected in this study. Considering the geometric illustration of an ellipsoidal particle (prolate spheroid) shown in Fig. 8, we set three semiaxis lengths as $c > a = b$. There were two independent variables required to define the geometry, equivalent particle radius $\bar{R} = (a^2c)^{1/3}$ and aspect ratio $\alpha = c/a$, which were selected as design variables. The third design variable was potential sweep rate v. The range of the three design variables is shown in Table IV. A spherical particle of radius r_0 = 5 μm was used in the experimental work of Uchida et al.,[18] thus, the range of equivalent particle radii was selected as a 20% perturbation around 5 μm. The aspect ratio range was selected based on the experimental observation of particle morphology by scanning electron microscope (SEM). The selected potential sweep rate gave a charge/discharge rate of 2.7–3.6 C, which falls into the range of high-power applications.

The two objective functions chosen in this study were the peak value of the cyclically varying maximum von Mises stress σ_{max} (in megapascal) and the time-averaged resistive heat generation rate $\dot{Q}_{r,avg}$ (in picowatts). In fatigue analysis, the mean value of the cy-

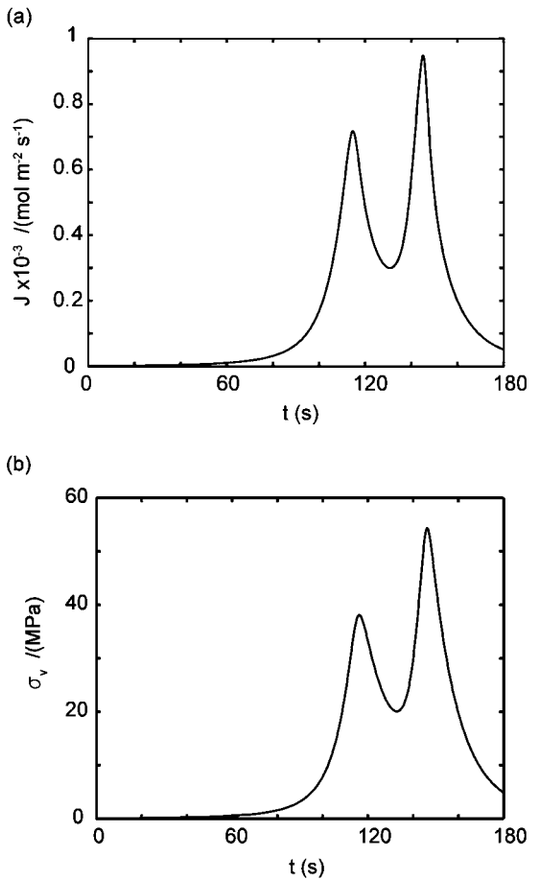

Figure 6. Simulation results of a spherical particle under 20 C charge: (a) Reaction flux on the particle surface, and (b) von Mises stress on the particle surface.

clically varying stress affects the number of cycles allowed before failure as well as the peak value.[43] In this study, numerical simulation results showed that mean stress and the peak value of the stress are highly correlated (the correlation coefficient is 0.992). Therefore, only the peak value of stress is considered as an objective function. Time-averaged resistive heat generation rate is the total resistive heat generation normalized by the overall charge half cycle time.

For the design of experiments, 20 points in total were selected in the design space defined in Table IV. Among these points, 15 of them are from FCCD and the remaining 5 points are from LHS. Numerical simulations were conducted on these 20 training points using the models described in the previous sections to obtain intercalation-induced stress and resistive heat.

Model construction and validation.— To construct the surrogate model using the obtained simulation results on the 20 training points, a second-order polynomial response surface was selected here. The coefficients in the approximation were determined by minimizing the error of approximation at the training points in the least-squares senses. The approximations obtained for the two objective functions were

$$\sigma_{max} = -18.0 + 4.81\bar{R} + 8.10\alpha + 4.13v - 0.065\bar{R}^2 - 0.275\bar{R}\alpha + 2.55\bar{R}v - 2.00\alpha^2 - 0.079\alpha v - 1.05v^2 \quad [13]$$

$$\dot{Q}_{r,avg} = 72.4 - 25.9\bar{R} + 5.29\alpha - 86.0v + 2.17\bar{R}^2 - 0.816\bar{R}\alpha + 18.1\bar{R}v - 0.018\alpha^2 - 3.09\alpha v + 18.9v^2 \quad [14]$$

The statistics of the response surface approximation are listed in Table V. RMS error is the difference between the prediction and simulation values on the training points. Adjusted coefficients of multiple determination R^2_{adj} are a measure of how well the approximation explains the variation of the objective functions caused by design variables. For a good fit, this coefficient should be close to one. PRESS is a cross-validation error. It is the summation of squares of all PRESS residues, each of which is calculated as the difference between the simulation by computer experiments and the prediction by the surrogate models constructed from the remaining sampling points excluding the point of interest itself.[42] As shown in Table V, the normalized rms error and PRESS are small, and the adjusted coefficients of multiple determination R^2_{adj} is very close to 1. Therefore, the surrogate models constructed approximate the objective functions quite well.

To further validate the accuracy of constructed surrogate models, they were tested by comparing the predicted and simulated values from computer experiments, on four testing points different from the training points. The results of the comparison show that the differences between the prediction and simulation results are within 6%.

To summarize, the surrogate models constructed, Eq. 13 and 14, not only explain the variation of objective functions resulting from design variables well, but also give a good prediction of the objective functions. Therefore, the obtained response surface approximations can be used with confidence to analyze dependencies among objective functions and design variables.

Analysis based on obtained surrogate models.— These dependencies are shown in Fig. 9. We note that (*i*) intercalation-induced stress σ_{max} increases with both increasing equivalent radius $\bar{R}$ and increasing potential sweep rate v. However, intercalation-induced stress σ_{max} increases first and then decreases as aspect ratio α increases; and (*ii*) time-averaged resistive heat generation rate $\dot{Q}_{r,avg}$ increases with both increasing equivalent radius $\bar{R}$ and increasing potential sweep rate v; however, time-averaged resistive heat generation rate $\dot{Q}_{r,avg}$ decreases as aspect ratio α increases. This surrogate-based analysis suggests that ellipsoidal particles with larger aspect ratios are superior to spherical particles in terms of improvement of the battery performance when stress and heat generation are the only limiting factors considered.

As pointed out earlier, intercalation-induced stress depends on the concentration distribution. When equivalent radius $\bar{R}$ increases, the range of concentration distributions within the particle becomes wider because of the longer diffusion path. Therefore, the intercalation-induced stress increases as equivalent radius $\bar{R}$ increases. When potential sweep rate v increases, the electrochemical reaction rate driven by the surface overpotential becomes faster, which results in large flux on the particle surface boundary. Therefore, one expects a larger concentration gradient inside the particle and larger intercalation-induced stress for larger potential sweep rate v. When aspect ratio α increases, there are two competing effects: the shorter semiaxis length a and b decrease and the longer semiaxis length c increases. The increase of the longer semiaxis leads to stress increase, and the decrease of the shorter semiaxis leads to stress decrease. Therefore, intercalation-induced stress increases first and then decreases as aspect ratio increases.

As shown in Eq. 10, resistive heat rate is the product of current and overpotential (or polarization), and the time-averaged heat generation rate over the charge half cycle is

$$\dot{Q}_{r,avg} = \frac{1}{\Delta t_{charge}} \int I(V - U^{avg}) dt \quad [15]$$

As the equivalent radius increases, the surface area subjected to reaction is larger, which results in larger total current. Therefore, the averaged resistive heat generation rate increases. When the potential sweep rate increases, the electrochemical reaction on the surface is driven faster, which results in larger polarization, or overpotential.

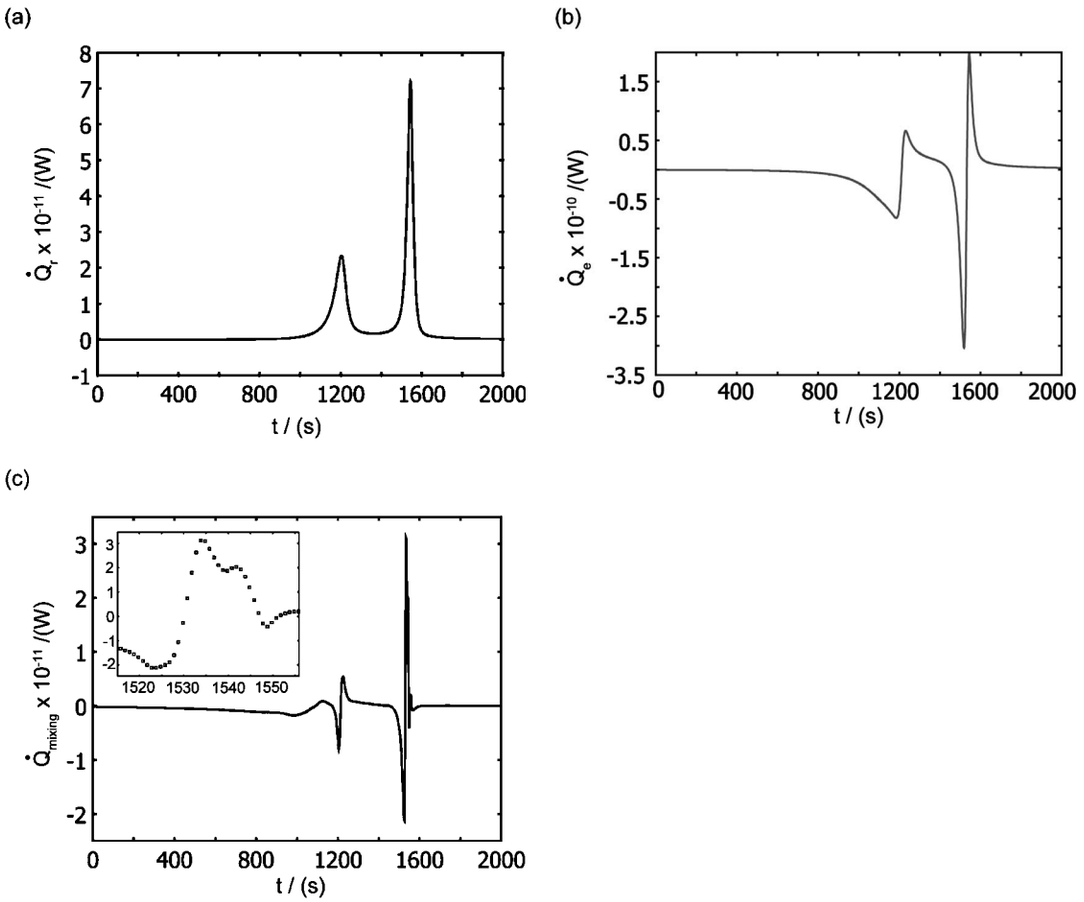

Figure 7. Simulation results of various heat generation sources during the charge half cycle: (a) Resistive heating, (b) entropic heating, and (c) heat of mixing.

Therefore, the averaged resistive heat generation rate increases even though the time duration for the charge half cycle decreases. When aspect ratio increases, the shorter semiaxis length decreases, which results in the decrease of average polarization or overpotential due to the shorter average diffusion path. Therefore, averaged resistive heat generation rate decreases.

Table III. Averaged heat generation rates during charge process.

	Case I	Case II
Potential sweep rate v	0.4 mV/s	1 mV/s
Charge time	2000 s	800 s
Heat of mixing	-7.55×10^{-14} W	-2.31×10^{-13} W
Resistive heating	2.88×10^{-12} W	1.63×10^{-11} W
Entropic heat	-4.88×10^{-12} W	-1.24×10^{-11} W

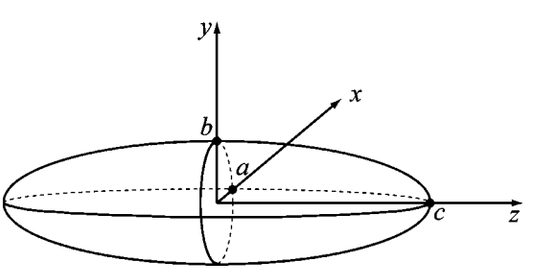

Figure 8. Geometric illustration of an ellipsoidal particle.

Global sensitivity analysis, which is often used to study the importance of design variables, was conducted to quantify the variation of the objective functions caused by three design variables. The importance of design variables is presented by a set of indices, main factor and total effect.[37] Main factor is the fraction of the total variance of the objective function contributed by a particular variable in

Table IV. Design variables and design space.

Name	Expression	Range
Equivalent radius	$\bar{R} = (a^2c)^{1/3}$	$4\ \mu m < \bar{R} < 6\ \mu m$
Aspect ratio	$\alpha = c/a$	$1 < \alpha < 3$
Potential sweep rate	v	$0.6\ mV/s < v < 0.8\ mV/s$

Table V. Evaluation of the response surface approximations.

Statistic name	Stress	Resistive heat
No. of training points	20	20
Minimum of data	11.7	1.96
Mean of data	19.9	8.86
Maximum of data	27.5	23.6
RMS error (normalized[a])	0.0368	0.0168
R^2_{adj}	0.984	0.996
PRESS (normalized[a])	0.0498	0.0356

[a] Note: RMS error and PRESS are both normalized by the range of the objective functions, that is, the difference between the maximum and the minimum of data.

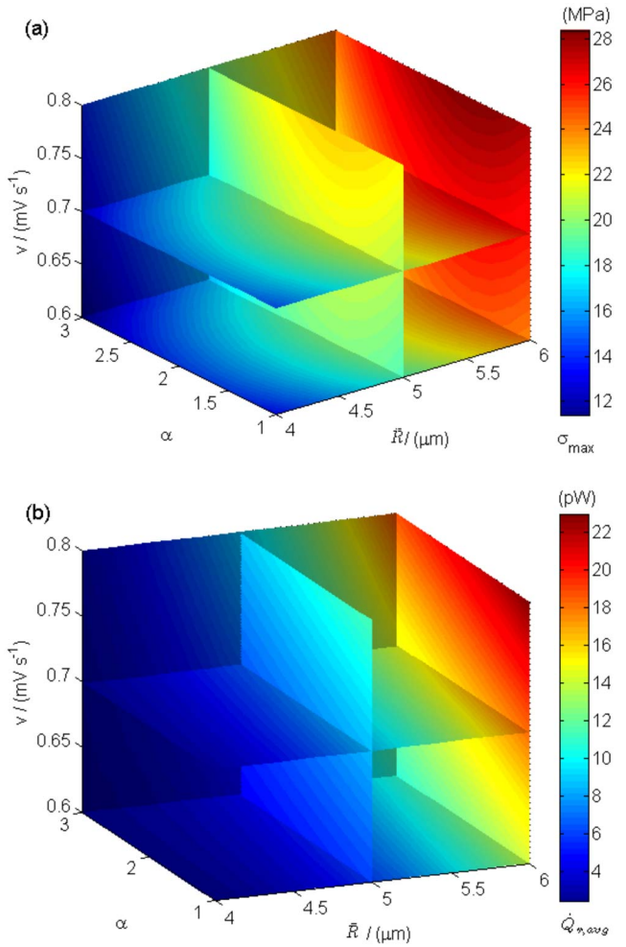

Figure 9. (Color online) Dependency between objective functions and design variables: (a) Maximum von Mises stress σ_{max} (in megapascal), and (b) time-averaged resistive heat rate $\dot{Q}_{r,avg}$ (in picowatts).

isolation, while the total effect includes contribution of all partial variances in which the variable of interest involved (basically by considering those interaction terms in the response surface approximation as shown in Eq. 13 and 14). The results of calculated total effect are listed in Table VI. It can be seen that equivalent particle radius contributes the most, for the design space range selected in Table IV, to the variation of the two objective functions, intercalation-induced stress and resistive heat (85 and 87% of total variation respectively).

Assumption of a Uniform Electric Potential

In the current model, electric potential inside the particle is assumed to be uniform, though potential varies in a battery electrode particle due to electric current flow within the particle. From a modeling standpoint, the most important value to accurately estimate is the electric potential on the particle surface because this value determines the electrochemical reaction rate via the Butler–Volmer equation. The simulation presented in this paper follows an earlier microelectrode experimental work, where an electric potential is applied through a filament in contact with a cathode particle.[18]

The potential distribution inside the particle could have been obtained numerically in our model by solving Poisson's equation. Experimentally,[18] potential was measured at a single point, but it is impractical to set up a similar boundary condition for the electric potential numerically because the applied potential is applied, ideally, at a single point. To evaluate the significance of potential variation on the particle surface to the intercalation process, we use a prescribed potential variation in the numerical simulation to investigate the significance of this variation.

The resistivity of $LiMn_2O_4$ is about 1.5×10^4 Ω cm.[44] The peak value measured current drawn from a 5 μm (radius) particle under 4 C discharge is on the order of 2 nA.[18] The electric potential variation inside a 5 μm (radius) particle under 4 C discharge is on the order of 10 mV, which is comparable to the surface overpotential obtained (Fig. 4). To evaluate the importance of this potential variation, we apply a prescribed electric potential to a 5 μm (radius) particle. Figure 10a shows the distribution of the potential at time instant $t = 1534$ s. The prescribed spatial potential variation follows the equation $0.005[x^2 + y^2 + (z - r_0)^2]/(2r_0)^2$, where r_0 (in microns) is the radius of the particle. Potentiodynamic control in this case has applied potential varying linearly with time.

Figures 10b-d show the simulation results of this case. The time history of von Mises (Fig. 10b) follows the same trend, when the potential is assumed to be uniform. The variation of electric potential results in a nonuniform distribution of surface overpotential and surface reaction flux, which, in turn, results in a shift in the concentration distribution as shown in Fig. 10c. However, the distribution pattern of von Mises stress is not altered; it remains axisymmetric as shown in Fig. 10d. The time instant of $t = 1534$ s is selected to present the results because this is the instant when von Mises stress reaches the temporal maximum value.

To sum up, although the variation of electric potential shifts the concentration distribution, it does not change von Mises stress distribution pattern. For simplicity and due to lack of more detailed empirical guideline, we assume that the electric potential is uniform inside the particle. Our finding does offer scientific insight into the interplay between stress and heat generation, particle geometry (aspect ratio and equivalent size), and potential sweep rate.

Table VI. Global sensitivity indices (total effect) for stress and resistive heat.

Variable	For stress	For resistive heat
Equivalent radius $\bar{R}$	0.851	0.873
Aspect ratio α	0.082	0.023
Potential sweep rate v	0.069	0.128

Conclusions

Intercalation-induced stress and heat generation inside Li-ion battery cathode ($LiMn_2O_4$) particles under potentiodynamic control were simulated. It was found that Li-ion concentration, surface flux, and intercalation-induced stress are highly correlated through the diffusion process, electrochemical kinetics, and the intercalation-induced lattice expansion. The two peaks observed in the flux and stress generation plots were attributable to intrinsic material properties (two plateaus in the OCP) and the applied potential. Three major heat generation sources, resistive heating, heat of mixing, and entropic heat, were analyzed. The heat of mixing was found to be negligible (two orders of magnitude smaller than the other two sources), and resistive heat was identified as the heating source of greatest importance.

The surrogate-based analysis approach was used to study the relationship among the two objective functions (intercalation-induced stress and resistive heat) and the selected design variables (particle morphology and the operating condition). It was shown that both intercalation-induced stress and time-averaged resistive heat generation rate increase with increasing equivalent particle radius and potential sweep rate; intercalation-induced stress increases first, then decreases, as the aspect ratio of an ellipsoidal particle increases, while averaged resistive heat generation rate decreases as aspect ratio increases. A sensitivity analysis was conducted to rank the importance of each design variable on the stress and heat generation. It was shown that particle equivalent radius contributes the most to

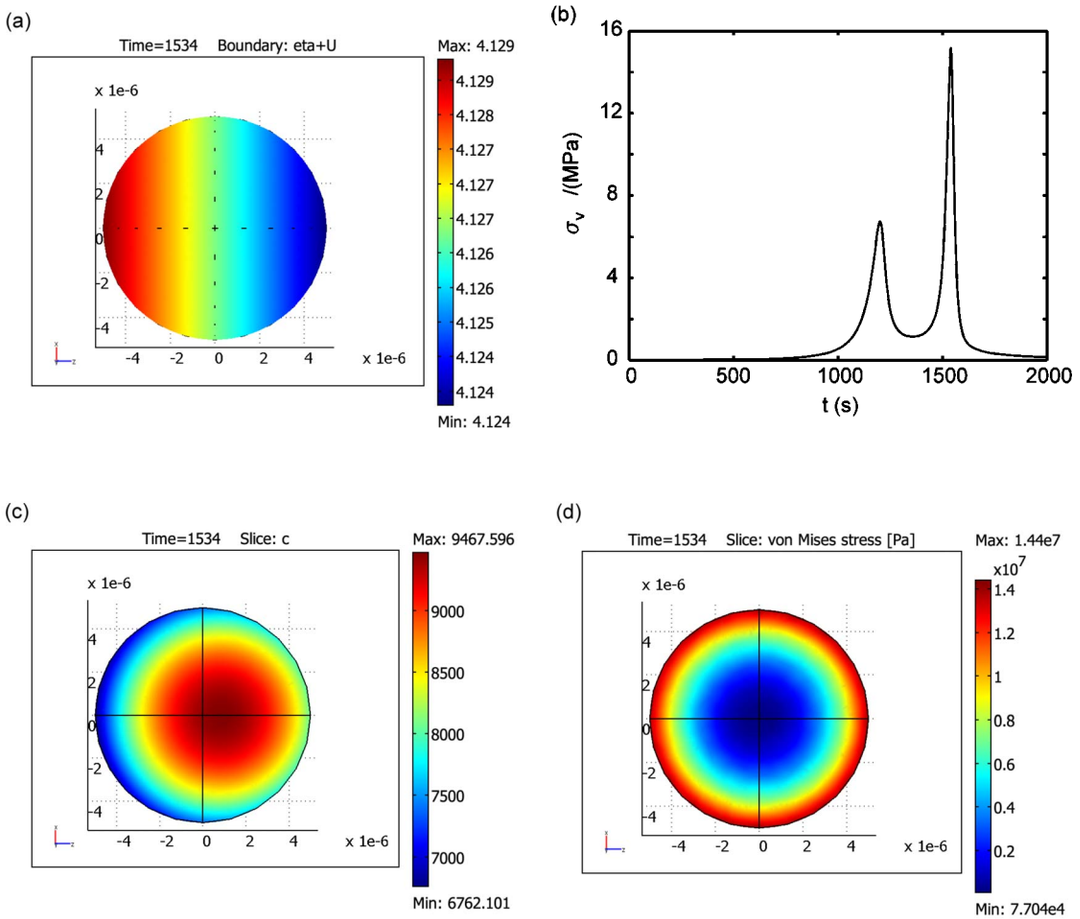

Figure 10. (Color online) Simulation with a predescribed potential variation: (a) Potential variation on particle surface at t = 1534 s, (b) time history of von Mises stress on particle surface, (c) concentration distribution inside the particle at t = 1534 s, and (d) von Mises stress distribution inside the particle at t = 1534 s.

both stress and heat generation for the design space range considered in this study (85 and 87% of the total variation, respectively). The observed variation trend from this systematic numerical study may also be explained from fundamental principles: intercalation-induced stress depends on the Li-ion concentration distribution and the resistive heat depends on a combination of total charge current and polarization (overpotential). The surrogate-based analysis conducted suggests that ellipsoidal particles with larger aspect ratios are preferred over spherical particles, in improving battery performance when stress and heat generation are the only factors considered.

The proposed models in this paper are only valid for purely active material ($LiMn_2O_4$) without inclusions. The obtained results are fundamental, but for homogeneous particles. The general methodology of surrogate-based analysis presented in this paper is extendable to consider more variables and geometries, such as more complicated geometric representation (aggregates) and applied potential profiles controlled by more parameters, or larger scales. For future work, we will extend the models developed here at the particle scale to the whole cell scale with a volume-averaging technique,[45-47] in which a multiscale modeling methodology[48] will be applied to pass the information obtained on the microscopic scale to the macroscale.

Acknowledgments

The surrogate modeling approach presented in this paper is supported by NASA under the Constellation University Institute Program (CUIP) (Claudia Meyer, program monitor). The electrochemical modeling in this work is supported by the U.S. Department of Energy through the BATT program (Dr. Tien Duong, program manager) and by the Ford Motor Company (Ted Miller and Kent Snyder, program managers). We also acknowledge our collaborators G. Liu, X.-Y. Song, and V. S. Battaglia, from Lawrence Berkeley National Laboratory, for providing SEM images of cathode particles, which were used to estimate aspect ratios.

University of Michigan assisted in meeting the publication costs of this article.

List of Symbols

a,b,c	lengths of the three semi-axes of ellipsoid, μm
c	concentration of lithium ions, mol m^{-3}
$\tilde{c}$	concentration change from initial value, mol m^{-3}
D	lithium diffusion coefficient, m^2 s^{-1}
E	Young's modulus, GPa
F	Faraday's constant, 96487 C mol^{-1}
ΔH	enthalpy of reaction. J mol^{-1}
$\bar{H}$	partial molar enthalpy, J mol^{-1}
I	current of cell, A
$\mathbf{i}_n(i_n)$	current density vector (scalar), A m^{-2}
i_0	exchange current density, A m^{-2}
$\mathbf{J}(J)$	species flux vector (scalar), mol m^{-2} s^{-1}
k	reaction constant, m$^{5/2}$ s^{-1} mol$^{-1/2}$
$\dot{Q}$	heat generation rate, W
R	gas constant, 8.314 J mol^{-1} K^{-1}
$\bar{R}$	equivalent radius of ellipsoidal particles, μm

R^2_{adj}	adjusted coefficient of multiple determination
r_0	particle radius, μm
r_k	rate of reaction k, mol s^{-1}
T	temperature, K
t	time, s
U	open circuit potential, V
U_H	enthalpy potential, V
V	potential of solid phase, V
v	potential sweep rate, mV s^{-1}
x,y,z	spatial coordinate, μm
y	state of charge

Greek symbols

α	aspect ratio
β	symmetry factor
ε_{ij}	strain
η	surface overpotential, V
ν	Poisson's ration
σ_{ij}	stress, Pa
Ω	partial molar volume, m^3 mol^{-1}

Subscripts

0	exchange current density i_0, particle radius r_0, initial concentration c_0
avg	time-averaged (heat generation rate)
e	entropic heat
g	heat generation
h	hydrostatic (stress)
i,j	index for tensor elements or index of species
k	index for a chemical reaction
l	concentration of Li-ion in the electrolyte
max	maximum
mixing	heat of mixing
r	resistive heating
rad	radial direction
s	concentration of Li-ion in the solid phase
tang	tangential direction
v	von Mises stress
θ	concentration of available vacant sites

Superscripts

avg	average over volume

References

1. K. E. Thomas and J. Newman, *J. Electrochem. Soc.*, **150**, A176 (2003).
2. H. Maleki, G. Deng, A. Anani, and J. Howard, *J. Electrochem. Soc.*, **146**, 3224 (1999).
3. A. Du Pasquier, F. Disma, T. Bowmer, A. S. Gozdz, G. Amatucci, and J.-M. Tarascon, *J. Electrochem. Soc.*, **145**, 472 (1998).
4. R. Spotnitz and J. Franklin, *J. Power Sources*, **113**, 81 (2003).
5. M.-R. Lim, W.-I. Cho, and K.-B. Kim, *J. Power Sources*, **92**, 168 (2001).
6. D. Wang, X. Wu, Z. Wang, and L. Chen, *J. Power Sources*, **140**, 125 (2005).
7. H. Wang, Y.-I. Jang, B. Huang, D. R. Sadoway, and Y.-M. Chiang, *J. Electrochem. Soc.*, **146**, 473 (1999).
8. Y.-M. Choi and S.-I. Pyun, *Solid State Ionics*, **99**, 173 (1997).
9. K. E. Aifantis and J. P. Dempsey, *J. Power Sources*, **143**, 203 (2005).
10. D. Bernardi, E. Pawlikowski, and J. Newman, *J. Electrochem. Soc.*, **132**, 5 (1985).
11. Y. Chen and J. W. Evans, *J. Electrochem. Soc.*, **141**, 2947 (1994).
12. S. C. Chen, C. C. Wan, and Y. Y. Wang, *J. Power Sources*, **140**, 111 (2005).
13. J. Christensen and J. Newman, *J. Solid State Electrochem.*, **10**, 293 (2006).
14. R. E. Garcia, Y.-M. Chiang, W. C. Carter, P. Limthongkul, and C. M. Bishop, *J. Electrochem. Soc.*, **152**, A255 (2005).
15. Y.-B. Yi, C.-W. Wang, and A. M. Sastry, *J. Electrochem. Soc.*, **151**, A1292 (2004).
16. X. Zhang, W. Shyy, and A. M. Sastry, *J. Electrochem. Soc.*, **154**, A910 (2007).
17. A. Guerfi, P. Charest, K. Kinoshita, M. Perrier, and K. Zaghib, *J. Power Sources*, **126**, 163 (2004).
18. I. Uchida, H. Fujiyoshi, and S. Waki, *J. Power Sources*, **68**, 139 (1997).
19. D. Zhang, B. N. Popov, and R. E. White, *J. Electrochem. Soc.*, **147**, 831 (2000).
20. K. E. Thomas, C. Bogatu, and J. Newman, *J. Electrochem. Soc.*, **148**, A570 (2001).
21. I. Taniguchi, C. K. Lim, D. Song, and M. Wakihara, *Solid State Ionics*, **146**, 239 (2002).
22. X. He, J. Li, Y. Cai, C. Jiang, and C. Wan, *Mater. Chem. Phys.*, **95**, 105 (2006).
23. W. Liu, G. C. Farrington, F. Chaput, and B. Dunn, *J. Electrochem. Soc.*, **143**, 879 (1996).
24. S. H. Ju, D. Y. Kim, E. B. Jo, and Y. C. Kang, *J. Mater. Sci.*, **42**, 5369 (2007).
25. M. G. Lazarraga, S. Mandal, J. Ibanez, J. M. Amarilla, and J. M. Rojo, *J. Power Sources*, **115**, 315 (2003).
26. L. Fransson, T. Eriksson, K. Edström, T. Gustafsson, and J. O. Thomas, *J. Power Sources*, **101**, 1 (2001).
27. A. Momchilov, A. Trifonova, B. Banov, B. Pourecheva, and A. Kozawa, *J. Power Sources*, **81–82** 566 (1999).
28. K. Zaghib, J. Shim, A. Guerfi, P. Charest, and K. A. Striebel, *Electrochem. Solid-State Lett.*, **8**, A207 (2005).
29. Y.-H. Chen, C.-W. Wang, G. Liu, X.-Y. Song, V. S. Battaglia, and A. M. Sastry, *J. Electrochem. Soc.*, **154**, A978 (2007).
30. T. H. Cho, S. M. Park, M. Yoshio, T. Hirai, and Y. Hideshima, *J. Power Sources*, **142**, 306 (2005).
31. M. Higuchi, K. Katayama, Y. Azuma, M. Yukawa, and M. Suhara, *J. Power Sources*, **119–121**, 258 (2003).
32. T. F. Fuller, M. Doyle, and J. Newman, *J. Electrochem. Soc.*, **141**, 1 (1994).
33. J. Newman and K. E. Thomas-Alyea, *Electrochemical Systems*, 3rd ed., pp. 209–212, John Wiley & Sons, Hoboken, NJ (2004).
34. M. Doyle, J. Newman, A. S. Gozdz, C. N. Schmutz, and J.-M. Tarascon, *J. Electrochem. Soc.*, **143**, 1890 (1996).
35. M. M. Thackeray, *Prog. Solid State Chem.*, **25**, 1 (1997).
36. C. de Boor, *Spline Toolbox 3 User's Guide*, p. 3.8, The MathWorks Inc., Natick, MA (2006).
37. N. V. Queipo, R. T. Haftka, W. Shyy, T. Goel, R. Vaidyanathan, and P. K. Tucker, *Prog. Aerosp. Sci.*, **41**, 1 (2005).
38. J. I. Madsen, W. Shyy, and R. T. Haftka, *AIAA J.*, **38**, 1512 (2000).
39. T. Goel, R. Vaidyanathan, R. T. Haftka, W. Shyy, N. V. Queipo, and K. Tucker, *Comput. Methods Appl. Mech. Eng.*, **196**, 879 (2007).
40. G. E. P. Box and K. B. Wilson, *J. R. Stat. Soc. Ser. B (Methodol.)*, **13**, 1 (1951).
41. M. D. McKay, R. J. Beckman, and W. J. Conover, *Technometrics*, **21**, 239 (1979).
42. R. H. Myers and D. C. Montgomery, *Response Surface Methodology: Process and Product Optimization Using Designed Experiments*, pp. 17–48, John Wiley & Sons, New York (1995).
43. N. E. Dowling, *Mechanical Behavior of Materials: Engineering Methods for Deformation, Fracture, and Fatigue*, 2nd ed., pp. 357–400, Prentice Hall, Upper Saddle River, NJ (1999).
44. Y. Shimakawa, T. Numata, and J. Tabuchi, *J. Solid State Chem.*, **131**, 138 (1997).
45. W. Shyy, S. S. Thakur, H. Ouyang, J. Liu, and E. Blosch, *Computational Techniques for Complex Transport Phenomena*, pp. 231–258, Cambridge University Press, Cambridge, England (1997).
46. A. R. Martin, C. Saltiel, and W. Shyy, *J. Heat Transfer*, **120**, 458 (1998).
47. E. Sozer and W. Shyy, Paper AIAA-2007-5549 presented at the 43rd AIAA/ASME/SAE/ASEE Joint Propulsion Conference and Exhibit, Cincinnati, 2007.
48. W. E, B. Engquist, X. Li, W. Ren, and E. Vanden-Eijnden, *Comm. Comp. Phys.*, **2**, 367 (2007).